Supporting information

Nanoparticle Fragmentation Below the Melting Point Under Single Picosecond Laser Pulse Stimulation

Peiyuan Kang[1], Yang Wang[1], Blake A. Wilson [1], Yaning Liu[1], Napat Dawkrajai[1], Jaona Randrianalisoa[2], Zhenpeng Qin[1, 3, 4, 5,] *

1. Department of Mechanical Engineering, University of Texas at Dallas, 800 West Campbell Road, Richardson, Texas 75080, United States.
2. Institut de Thermique, Mécanique, Matériaux (ITheMM EA 7548), University of Reims Champagne–Ardenne, Reims, Cedex 2 51687, France.
3. Department of Bioengineering, University of Texas at Dallas, 800 West Campbell Road, Richardson, Texas 75080, United States.
4. Center for Advanced Pain Studies, University of Texas at Dallas, 800 West Campbell Road, Richardson, Texas 75080, United States.
5. Department of Surgery, University of Texas at Southwestern Medical Center, 5323 Harry Hines Boulevard, Dallas, Texas 75390, United States.

This PDF file includes:

Figs. S1 to S9
Tables S1 to S3
References (1 to 19, also included in paper)

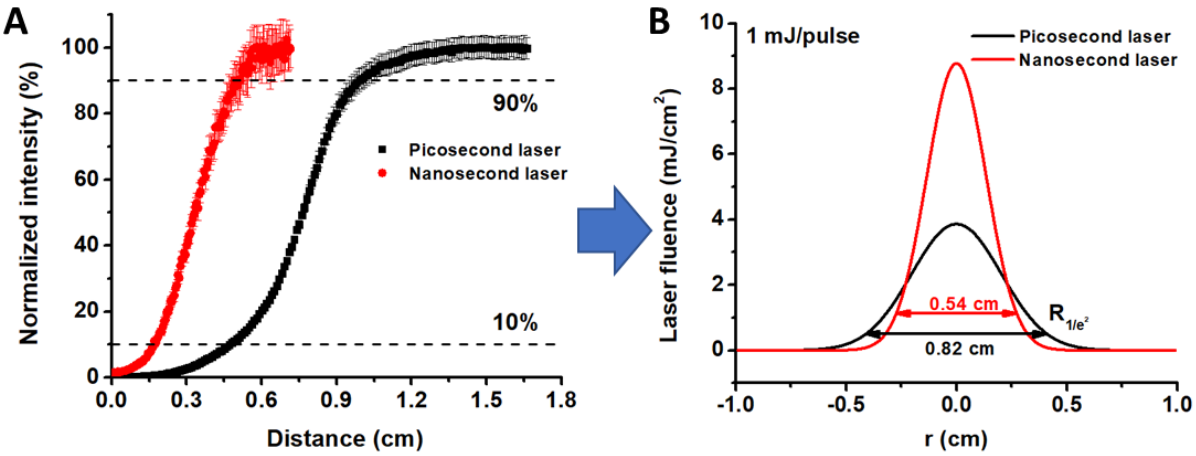

Figure S1. Laser beam profile measurement (A) Blade-edge measurement of laser beam profile for nanosecond and picosecond laser beam. (B) Gaussian laser beam profile for nanosecond and picosecond laser.

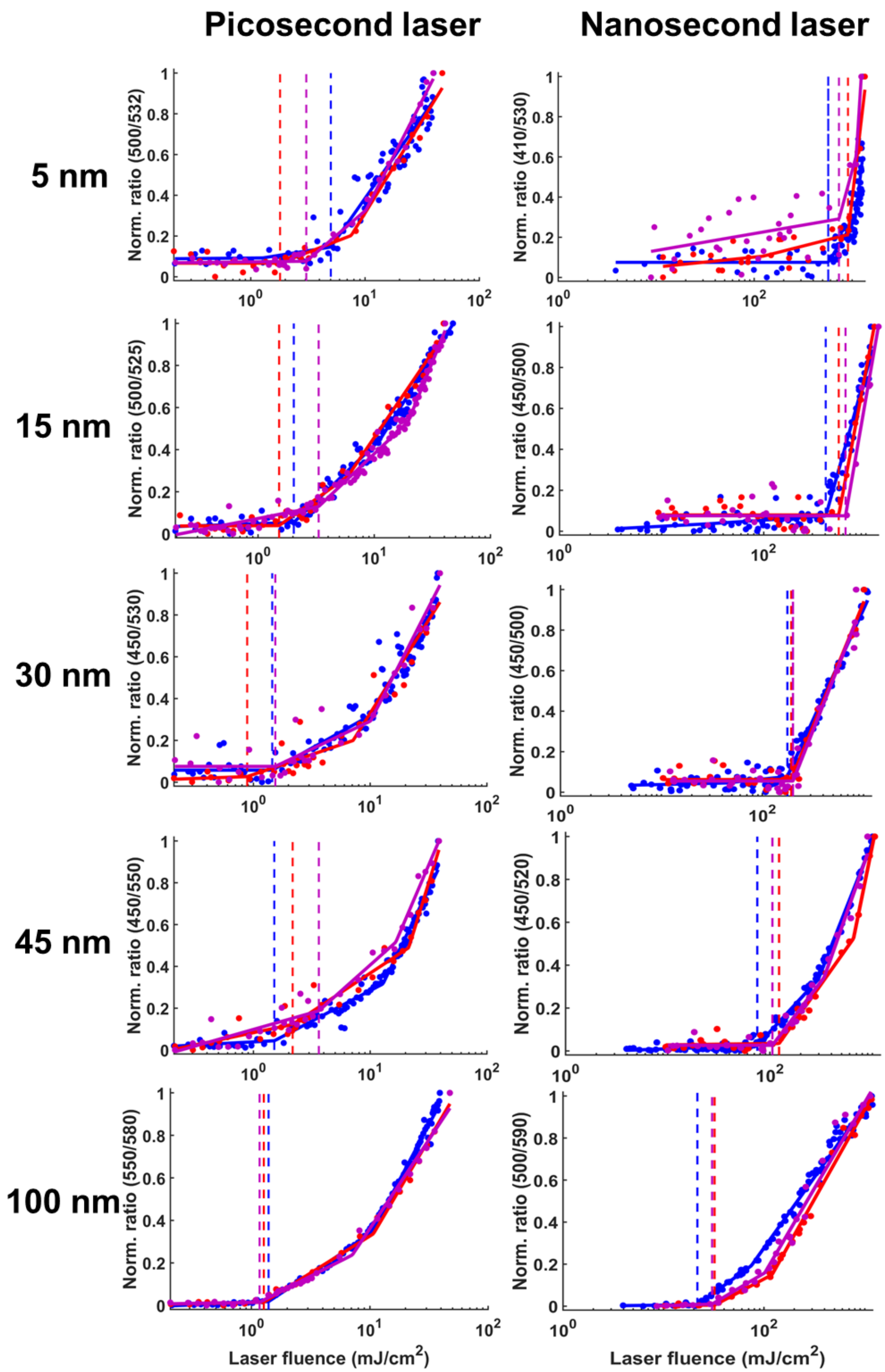

Figure S2. Extinction analysis for different particle sizes. The left panel is picosecond laser induced fragmentation. The right panel is nanosecond laser induced fragmentation. Different color of data is obtained from different experiments.

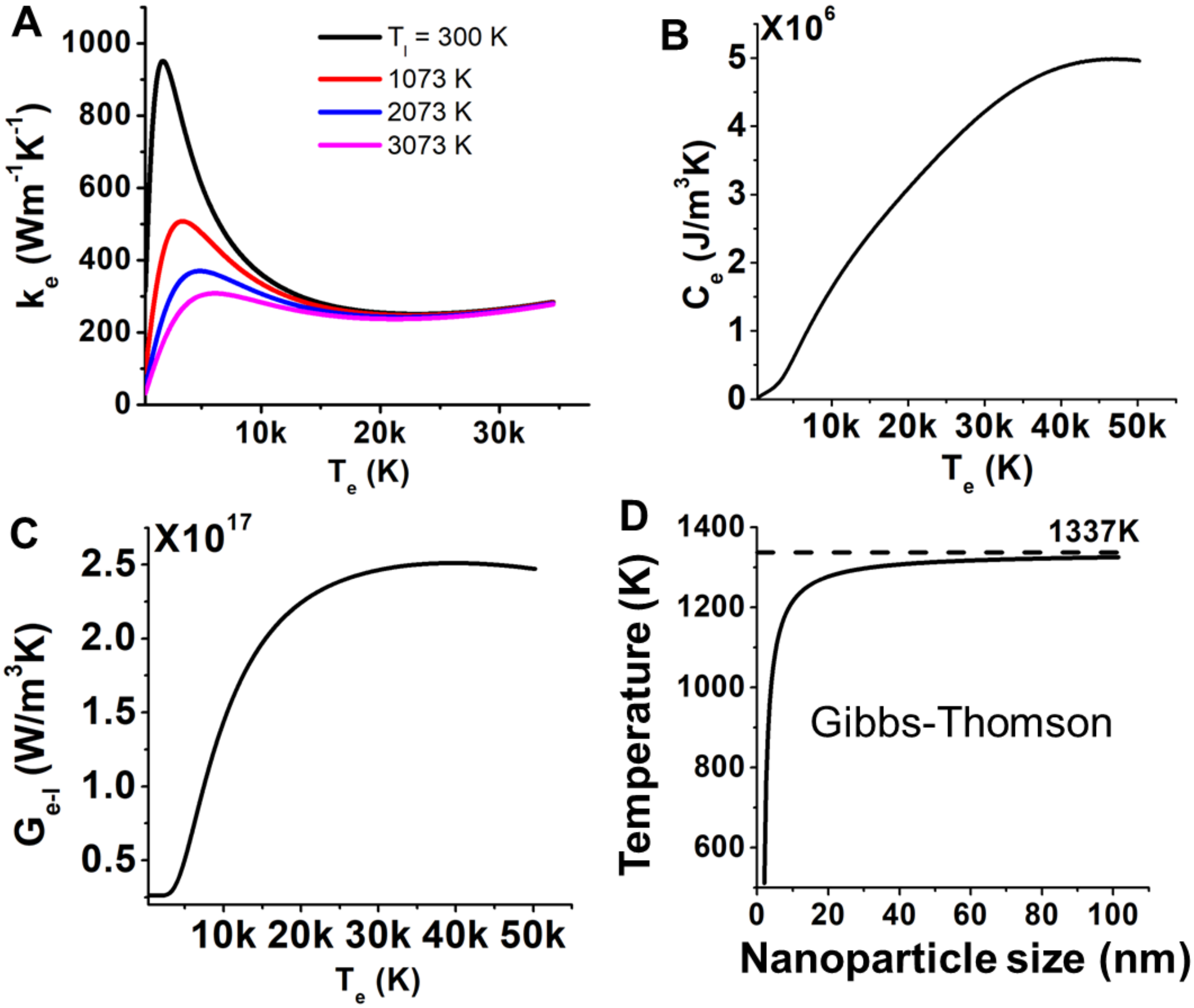

Figure S3. Material properties for two temperature model. (A) Thermal conductivity of electrons changes with electron temperature (T_e) and lattice temperature (T_l). (B) Specific heat of electron. (C) Electron-phonon coupling factor (G_{e-l}). (D) Size dependent melting point for gold nanoparticles calculated by Gibbs-Thomson equation.

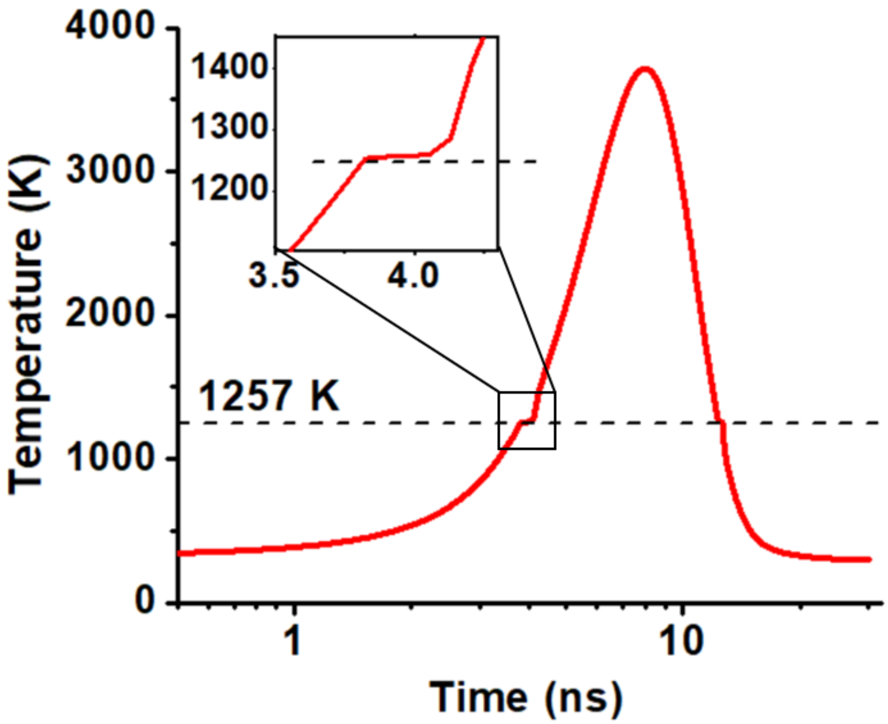

Figure S4. Temperature evolution for 15 nm AuNP under the ns laser in figure 3A. The phase transition occurs at 1257 K as the gold melts.

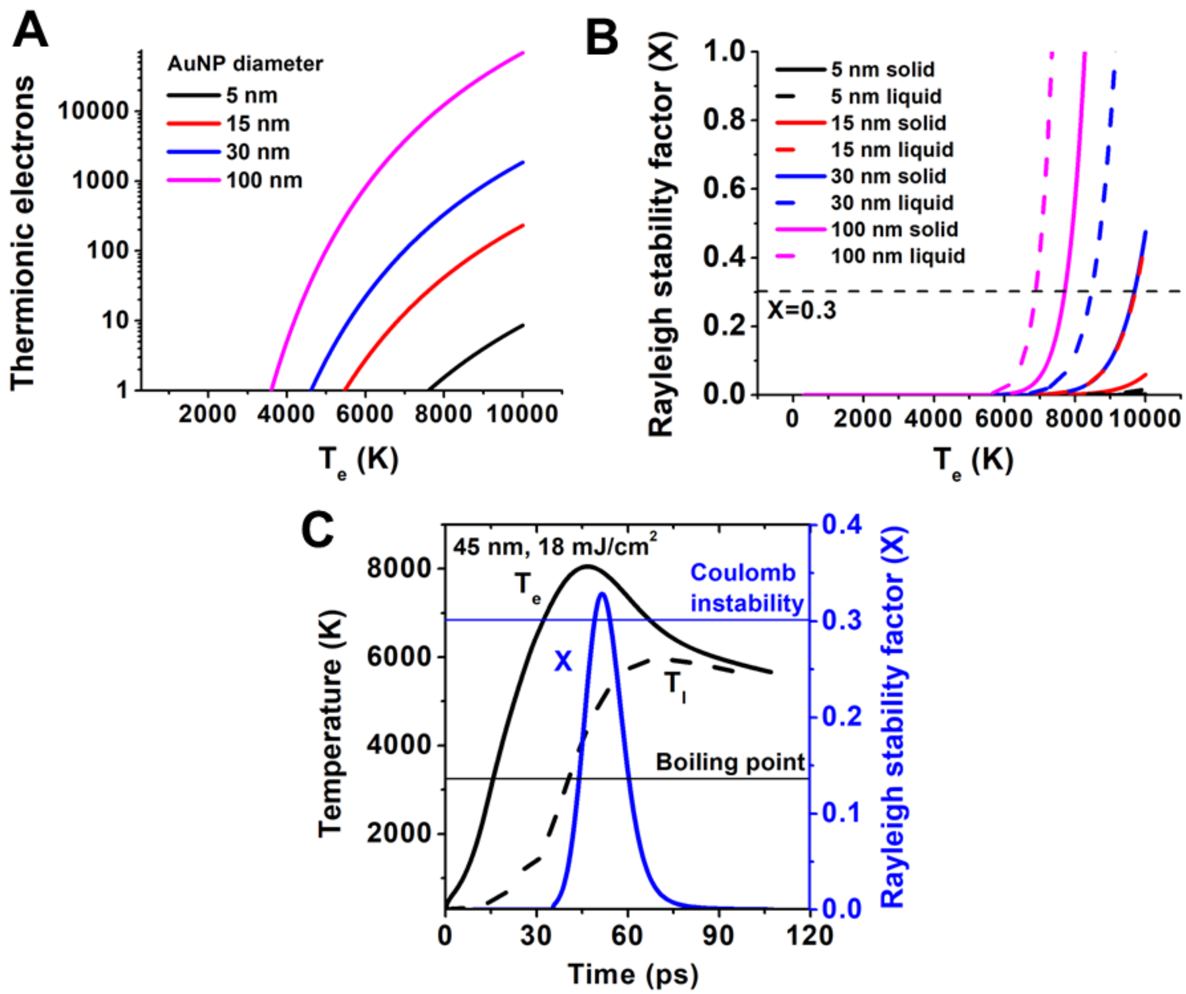

Figure S5. Parameters for the Rayleigh instability model. (A) The thermionic electrons and (B) Rayleigh stability factor (X) as a function of electron temperature (T_e). (C) Evolution of temperature and X for 45 nm gold nanosphere (AuNP). X is larger than 0.3 when laser fluence is 18 mJ/cm^2.

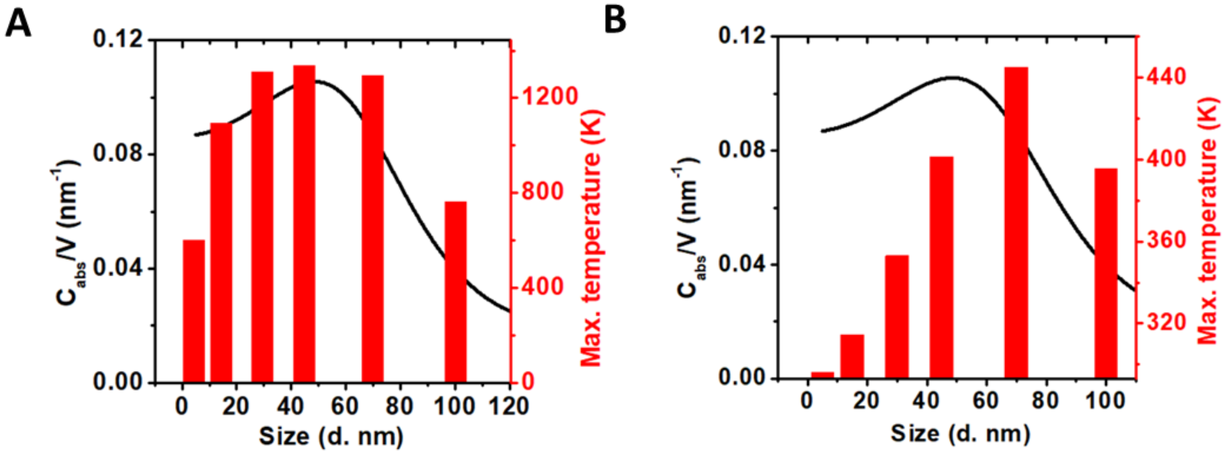

Figure S6. Volumetric heating factor and the maximum temperature of gold lattice for (A) picosecond laser and (B) nanosecond laser heating. C_{abs} is absorption cross section area and V is volume of NP. C_{abs}/V represents amount of light energy absorbed by the particle per volume. The laser fluence is the same for both cases (3.16 mJ/cm^2).

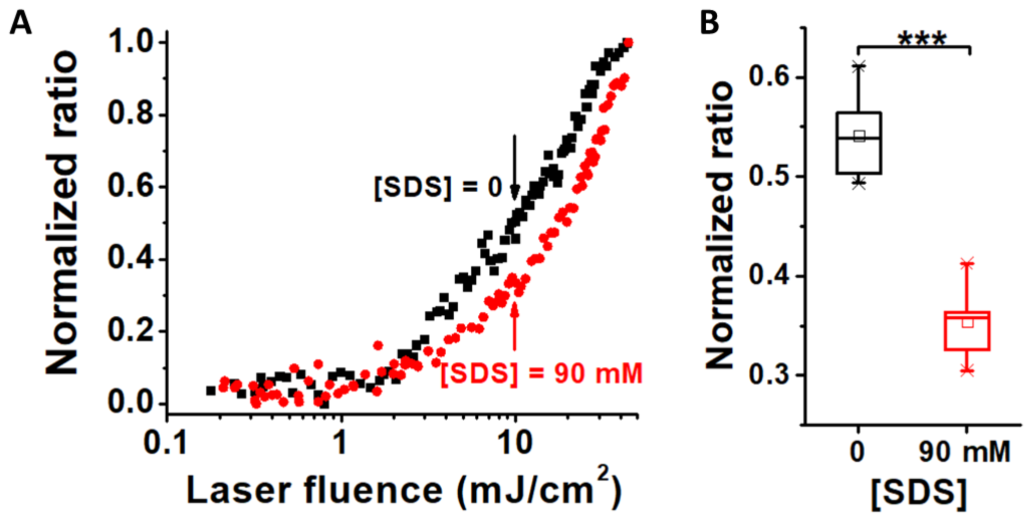

Figure S7. Influence of sodium dodecyl sulfate (SDS) on picosecond laser fragmentation. (A) Extinction analysis for picosecond laser ablation for 15 nm AuNP in 90 mM SDS solution (red dots) and in water (black dots). Picosecond laser ablation can be delayed by addition of SDS. (B) Comparison of normalized ratio at 10 mJ/cm^2 for AuNP ablation in water and in 90 mM SDS (n=6). - indicate maximum and minimum data, X indicates 99% and 1% confidence, □ represents the mean value, box and bars represent 25%, 75% confidence and the median value. *** indicates $p<0.05$.

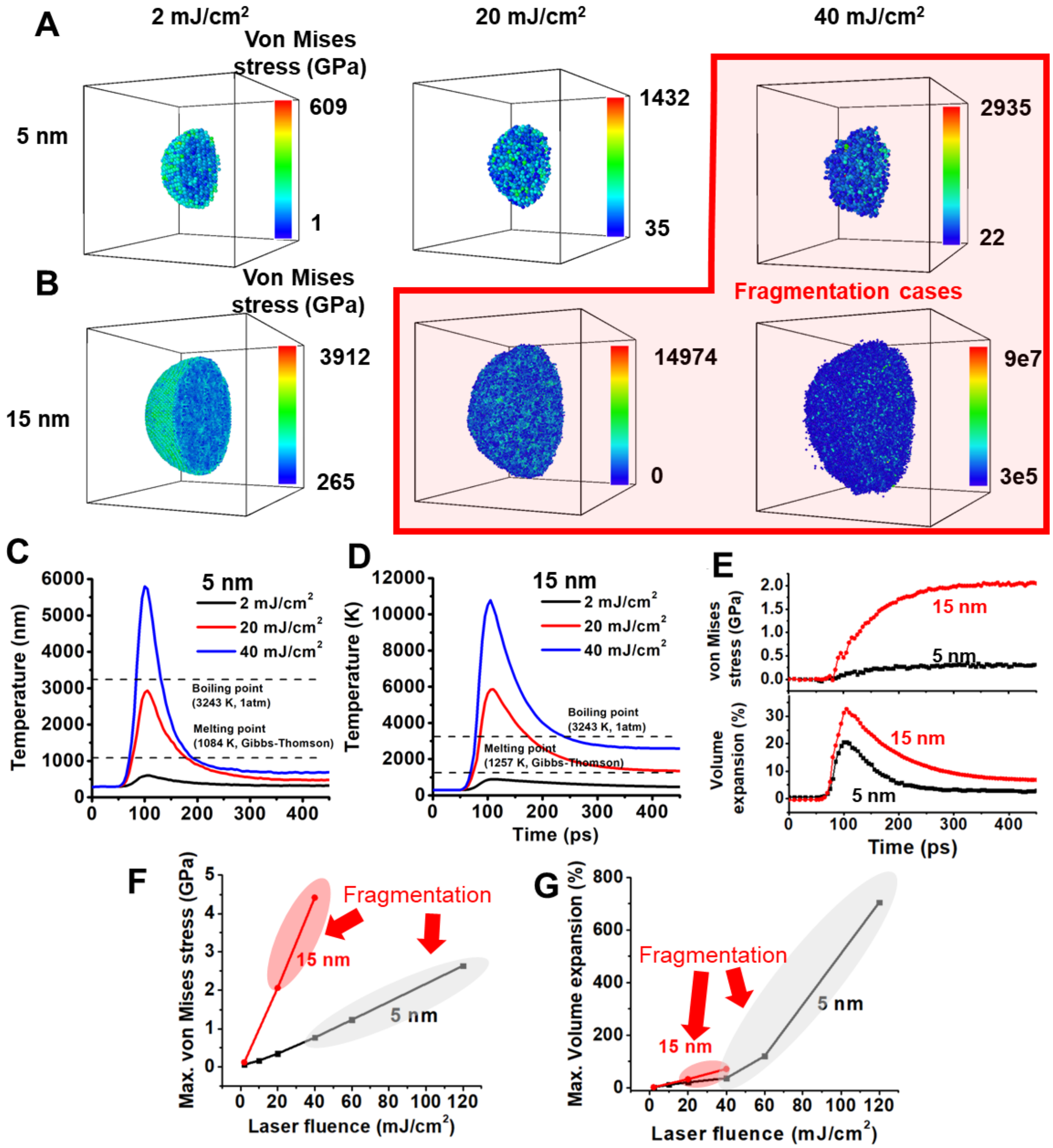

Figure S8. Molecular dynamics simulation for fragmentation of AuNP. The contour plot of von Mises stress of (A) 5 nm AuNP and (B) 15 nm AuNP with the cross section cutting through the center of AuNP when the particle reaches maximum temperature. Daughter particles were observed when laser intensity is larger than 40 mJ/cm^2 for 5 nm AuNP and 20 mJ/cm^2 for 15 nm AuNP. (C-D) The average gold temperature for (C) 5 nm AuNP and (D) 15 nm AuNP. The melting point and boiling point are marked with dashed lines. (E) The average von Mises stress and volume expansion for 5 nm (black) and 15 nm (red) AuNP with the laser intensity of 20 mJ/cm2. (F) Maximum von Mises stress for different laser intensities. (G) Maximum volume expansion for different laser intensities. The fragmentation cases are marked with red (15 nm AuNP) and gray shaded area (5 nm AuNP).

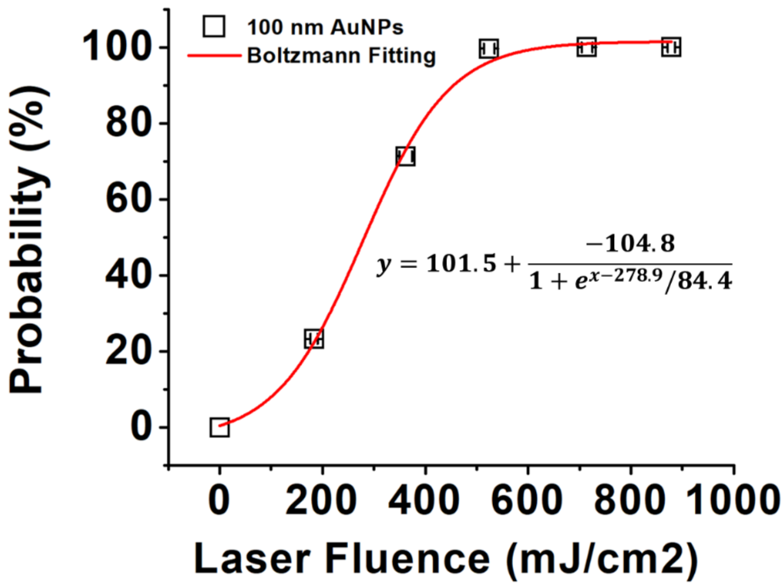

Figure S9. The probability of vapor nanobubble generation measured by an optical pump-probe setup. At the fragmentation threshold of 100 nm AuNP (1.3 mJ/cm^2), the vapor nanobubble generation probability is less than 1%.

Table S1. Parameters in TTM model and MD simulation

Parameters	Value	Unit	Ref.
Thermal conductivity of electron K_e	$K_e = \chi \frac{(\phi_e{}^2+0.16)^{5/4}(\phi_e{}^2+0.44)\phi_e}{(\phi_e{}^2+0.092)^{1/2}(\phi_e{}^2+0.16\phi_l)}$	W/(m·K)	1
Normalized electron temperature, φ_e	$\phi_e = T_e/T_f$	1	1
Normalized electron temperature, φ_l	$\phi_l = T_l/T_f$	1	1
Fermi temperature, T_f	64200	K	1
Thermal conductivity of lattice, K_l	2	W/(m·K)	2
Thermal conductivity of water, K_m	K_m = -0.9003748+0.008387698×T^1-1.118205×10^{-5}×T^2	W/(m·K)	3
Specific heat of electron, C_e	From VSAP	J/(kg·K)	4
Specific heat of lattice, C_l	129 for solid, 163 for liquid	J/(kg·K)	3
Specific heat of water, C_m	4035.841+0.492312×T^1 for T_m<373K, 4219 for T_m>373K	J/(kg·K)	3
Density of gold, ρ_{Au}	19501.44-0.6933844×T^1-2.041944×$10^{-4}$$T^2$+4.297982×$10^{-8}$$T^3$ ~19300 for 86K<T_l<1338K 19033-1.4434×T for 1338K<T_l<3080K 14587.4 for T_l>3080K	kg/m^3	3
Bulk melting temperature, T_m^*	1337	K	3
Interface tension between liquid and solid gold, σ_{sl}	0.27	N/m	5
Density of water, ρ_m	972.7584+0.2084×T^1-4.0×10^{-4}×T^2 for 273K<T_m<283K 345.28+5.749816×T^1-0.0157244×T^2+1.264375×10^{-5}×T^3 for 283K<T_m<373K 958 for T_m>373K	kg/m^3	3
Electron-phonon coupling factor, $G_{e\text{-}l}$	Calculated from VASP	W/(m^3·K)	4
Interfacial thermal conductance, h	105×10^6	W/(m^2·K)	6
Electron density of states, EDOS	Calculated from VASP	1/(cm^3·eV^1)	4
Chemical potential, µ	Calculated from VASP	J/kg	4
Boltzmann constant, k_B	1.38×10^{-23}	m^2·kg/(s^2·K)	1
Unit cell edge length of gold, a_{fcc}	4.08	Å	7
Volume of AuNP, V_{NP}	$V_{NP} = {}^4/_3\, \pi R_{NP}{}^3$	nm^3	7

Radius of AuNP, R_{NP}	5~100	nm	
Wigner-Seitz radius, r_{ws}	1.65×10^{-8}	cm	7
Surface tension of gold, σ	8.78 for T_l<1337 $1.15-1.4\times(T_l-1337)\times10^{-4}$ for T_l>1337	N/m	8-9
Elementary charge, e	4.803204×10^{-10}	stat C	7
Stretching stiffness, K_s	450.00	kcal/(mol·Å^2)	10-12
Equilibrium bond length, r_0	0.9572	Å	10-12
Bending stiffness, K_Θ	55.00	kcal/(mol·rad^2)	10-12
Equilibrium angle, Θ_0	104.52	degree	10-12
Partial atomic charge of O, q_O	-0.83	C	10-12
Partial atomic charge of H, q_H	0.415	C	10-12
Well-depth of OO bond, ε_{OO}	0.102	kcal/mol	10-12
LJ radius of OO bond, σ_{OO}	3.188	Å	10-12
Well-depth of AuO bond, ε_{AuO}	0.59	kcal/mol	10-12
LJ radius of AuO bond, σ_{AuO}	3.6	Å	10-12

Note: The bond energy ε and bond length σ for HH, OH, and AuH are set to 0.

Table S2. Previous reported laser fluence of ps laser fragmentation for plasmonic nanoparticles.

Wavelength	Pulse duration	Material, diameter	Ligand	Fluence	Reference
355 nm	30 ps	Au, 25 nm	Citrate	14 mJ/cm^2	13
532 nm	10 ps	Au, 53 nm	No	30 mJ/cm^2	14
400 nm	0.15 ps	Au, 50 nm	Citrate	6 mJ/cm^2	15
355 nm	15 ps	Au, 59 nm	Citrate	19.6 mJ/cm^2	16
355 nm	18 ps	Ag, 65 nm	Citrate	7.5 mJ/cm^2	17
1070 nm	5 ps	Ag, 25 nm	No	0.13 mJ/cm^2	18
532 nm	10 ps	Au, 54 nm	No	>10 mJ/cm^2	19
532 nm	28 ps	Au, 5~100 nm	Citrate	1~2 mJ/cm^2	This study

Table S3. Estimation of particle sizes after a layer of molten material is ejected from the surface and form one daughter particles.

Original particle diameter (d_{NP})	Molten layer thickness at the surface melting temperature (L_{liq})	Model expectation of average large daughter particle size (d_{large})	Experimental observation of average large daughter particle size (d_{large})	Model expectation of average small daughter particle size (d_{small})	Experimental observation expectation of average small daughter particle size (d_{small})
5.6 nm	0.3 nm	5.3 nm	6.0 nm	1.2 nm	1.5 nm
15.4 nm	0.8 nm	14.6 nm	14.9 nm	3.2 nm	3.8 nm
102.6 nm	2.1 nm	100.5 nm	97.5 nm	15.8 nm	14.9 nm

References:

1. Chen, J. K.; Beraun, J. E.; Tham, C. L., Investigation of Thermal Response Caused by Pulse Laser Heating. *Numer. Heat Transfer, Part A* **2003,** *44* (7), 705-722.

2. Jain, A.; McGaughey, A. J. H., Thermal Transport by Phonons and Electrons in Aluminum, Silver, and Gold from First Principles. *Phys. Rev. B* **2016,** *93* (8), 081206.

3. COMSOL. Inc Comsol Multiphysics® Reference Manual, Version 5.3. www.comsol.com.

4. Lin, Z.; Zhigilei, L. V.; Celli, V., Electron-Phonon Coupling and Electron Heat Capacity of Metals under Conditions of Strong Electron-Phonon Nonequilibrium. *Phys. Rev. B* **2008,** *77* (075133).

5. Font, F.; Myers, T. G., Spherically Symmetric Nanoparticle Melting with a Variable Phase Change Temperature. *J. Nanopart. Res.* **2013,** *15* (12), 2086.

6. Plech, A.; Kotaidis, V.; Gresillon, S.; Dahmen, C.; von Plessen, G., Laser-Induced Heating and Melting of Gold Nanoparticles Studied by Time-Resolved X-Ray Scattering. *Phys. Rev. B* **2004,** *70*, 195423.

7. Giammanco, F.; Giorgetti, E.; Marsili, P.; Giusti, A., Experimental and Theoretical Analysis of Photofragmentation of Au Nanoparticles by Picosecond Laser Radiation. *J. Phys. Chem* **2010,** *114*, 3354-3363.

8. Nanda, K. K.; Maisels, A.; Kruis, F. E., Surface Tension and Sintering of Free Gold Nanoparticles. *J. Phys. Chem. C* **2008,** *112* (35), 13488-13491.

9. Egry, I.; Lohoefer, G.; Jacobs, G., Surface Tension of Liquid Metals: Results from Measurements on Ground and in Space. *Phys. Rev. Lett.* **1995,** *75* (22), 4043-4046.

10. MacKerell, A. D.; Bashford, D.; Bellott, M.; Dunbrack, R. L.; Evanseck, J. D.; Field, M. J.; Fischer, S.; Gao, J.; Guo, H.; Ha, S., *et al.*, All-Atom Empirical Potential for Molecular Modeling and Dynamics Studies of Proteins. *J. Phys. Chem. B* **1998,** *102* (18), 3586-3616.

11. Jorgensen, W. L.; Chandrasekhar, J.; Madura, J. D.; Impey, R. W.; Klein, M. L., Comparison of Simple Potential Functions for Simulating Liquid Water. *J. Chem. Phys.* **1983,** *79* (2), 926-935.

12. Price, D. J.; III, C. L. B., A Modified Tip3p Water Potential for Simulation with Ewald Summation. *The Journal of Chemical Physics* **2004,** *121* (20), 10096-10103.

13. Inasawa, S.; Sugiyama, M.; Yamaguchi, Y., Bimodal Size Distribution of Gold Nanoparticles under Picosecond Laser Pulses. *J. Phys. Chem. B* **2005,** *109* (19), 9404-9410.

14. Ziefuß, A. R.; Reichenberger, S.; Rehbock, C.; Chakraborty, I.; Gharib, M.; Parak, W. J.; Barcikowski, S., Laser Fragmentation of Colloidal Gold Nanoparticles with High-Intensity Nanosecond Pulses Is Driven by a Single-Step Fragmentation Mechanism with a Defined Educt Particle-Size Threshold. *J. Phys. Chem. C* **2018,** *122* (38), 22125-22136.

15. Werner, D.; Furube, A.; Okamoto, T.; Hashimoto, S., Femtosecond Laser-Induced Size Reduction of Aqueous Gold Nanoparticles: In Situ and Pump−Probe Spectroscopy Investigations Revealing Coulomb Explosion. *J. Phys. Chem. C* **2011,** *115* (17), 8503-8512.

16. Hashimoto, S.; Katayama, T.; Setoura, K.; Strasser, M.; Uwada, T.; Miyasaka, H., Laser-Driven Phase Transitions in Aqueous Colloidal Gold Nanoparticles under High Pressure: Picosecond Pump-Probe Study. *Phys. Chem. Chem. Phys.* **2016,** *18* (6), 4994-5004.

17. Kamat, P. V.; Flumiani, M.; Hartland, G. V., Picosecond Dynamics of Silver Nanoclusters. Photoejection of Electrons and Fragmentation. *J. Phys. Chem. B* **1998,** *102* (17), 3123-3128.

18. Jeon, J.-W.; Yoon, S.; Choi, H. W.; Kim, J.; Farson, D.; Cho, S.-H., The Effect of Laser Pulse Widths on Laser—Ag Nanoparticle Interaction: Femto- to Nanosecond Lasers. *Applied Sciences* **2018,** *8* (1), 112.

19. Ziefuss, A. R.; Reich, S.; Reichenberger, S.; Levantino, M.; Plech, A., *In Situ* Structural Kinetics of Picosecond Laser-Induced Heating and Fragmentation of Colloidal Gold Spheres. *Phys. Chem. Chem. Phys.* **2020,** *22*, 4993-5001.